Pulsed and CW Gaussian beam interactions with double negative metamaterial slabs

Richard W. Ziolkowski

Department of Electrical and Computer Engineering, University of Arizona, Tucson, AZ 85721 USA
ziolkowski@ece.arizona.edu

Abstract: The interactions of pulsed and continuous wave (CW) Gaussian beams with double negative (DNG) metatmaterials are considered. Sub-wavelength focusing of a diverging, normally incident pulsed Gaussian beam with a planar DNG slab is demonstrated. The negative angle of refraction behavior associated with the negative index of refraction exhibited by DNG metamaterials is demonstrated. The transmitted beam resulting from both 3-cycle and CW Gaussian beams that are obliquely incident on a DNG slab are shown to have this property. Gaussian beams that undergo total internal reflection from a DNG metamaterial slab are also shown to experience a negative Goos-Hänchen (lateral) shift. Several potential applications for these effects in the microwave and optical regimes are discussed.

OCIS codes: (260.2110) Electromagnetic Theory; (340.5500) Propagation; (350.5730) Resolution; (320.7120) Ultrafast phenomena; (999.9999) Metamaterials.

References and links

1. A. Ishimaru, *Electromagnetic Wave Propagation, Radiation, and Scattering*, (Prentice Hall, Englewood Cliffs, NJ, 1991), pp. 36-38.
2. V. G. Veselago, "The electrodynamics of substances with simultaneously negative values of ε and μ," Sov. Phys. Usp. **10**, 509-514 (1968).
3. D. R. Smith, W. J. Padilla, D. C. Vier, S. C. Nemat-Nasser, and S. Schultz, "Composite Medium with zimultaneously negative permeability and permittivity," Phys. Rev. Lett. **84**, 4184-4187 (2000).
4. J. B. Pendry, "Negative Refraction Makes a Perfect Lens," Phys. Rev. Lett. **85**, 3966-3969 (2000).
5. D. R. Smith and N. Kroll, "Negative refractive index in left-handed materials," Phys. Rev. Lett. **85**, 2933-2936 (2000).
6. R. A. Shelby, D. R. Smith, S. C. Nemat-Nasser, and S. Schultz, "Microwave transmission through a two-dimensional, isotropic, left-handed metamaterial," Appl. Phys. Lett. **78**, 489-491 (2001).
7. A. Shelby, D. R. Smith, and S. Schultz, "Experimental verification of a negative refractive index of refraction," Science **292**, 77-79 (2001).
8. R. W. Ziolkowski and E. Heyman, "Wave propagation in media having negative permittivity and permeability," Phys. Rev. E **64**, 056625 (2001).
9. C. Caloz, C.-C. Chang and T. Itoh, "Full-wave verification of the fundamental properties of left-handed materials in waveguide configurations," J. Appl. Phys. **90**, 5483-5486 (2001).
10. J. A. Kong, B.-I. Wu and Y. Zhang, "A unique lateral displacement of a Gaussian beam transmitted through a slab with negative permittivity and permeability," Microwave Opt. Tech. Lett. **33**, 136-139 (2002).
11. P. M. Valanju, R. M. Walter, and A. P. Valanju, "Wave refraction in negative-index media: Always positive and very inhomogeneous," Phys. Rev. Lett. **88**, 187401 (2002).
12. G. V. Eleftheriades, A. K. Iyer and P. C. Kremer, "Planar negative refractive index media using periodically L-C loaded transmission lines," IEEE Trans. Microwave Theory Tech. **50**, 2702-2712 (2002).
13. K. G. Balmain, A. A. Luttgen, and P. C. Kremer, "Resonance cone formation, reflection, refraction and focusing in a planar, anisotropic metamaterial," Proceedings of the URSI National Radio Science Meeting, pp. 45, San Antonio, TX, July 2002.
14. R. W. Ziolkowski, "Design, fabrication, and testing of double negative metamaterials," to appear in IEEE Trans. Antennas Propagat., June 2003.
15. A. Taflove, *Computational Electrodynamics*: *The Finite-Difference Time-Domain Method*, (Artech House, Inc., Norwood, MA, 1995).
16. A. Taflove, Ed., *Advances in Computational Electrodynamics: The Finite-Difference Time-Domain Method*, (Artech House, Inc., Norwood, MA, 1998).

#2157 - $15.00 US Received February 03, 2003; Revised March 18, 2003

17. D. C. Wittwer and R. W. Ziolkowski, "Two time-derivative Lorentz material (2TDLM) formulation of a Maxwellian absorbing layer matched to a lossy media," IEEE Trans. Antennas and Propagat. **48**, 192-199 (2000).
18. D. C. Wittwer and R. W. Ziolkowski, "Maxwellian material based absorbing boundary conditions for lossy media in 3D," IEEE Trans. Antennas and Propagat. **48**, 200-213 (2000).
19. J. B. Judkins, C. W. Haggans, and R. W. Ziolkowski, "2D-FDTD simulation for rewritable optical disk surface structure design," *Special Issue of Applied Optics on Optical Data Storage Technologies*, Appl. Opt. **35**, 2477-2487 (1996).
20. M. W. Feise, P. J. Bevelacqua, and J. B. Schneider, "Effects of surface waves on behavior of perfect lenses," Phys. Rev. B **66**, 035113 (2002).
21. A. Ishimaru and J. Thomas, "Transmission and focusing of a slab of negative refractive index," Proceedings of the URSI National Radio Science Meeting, pp. 43, San Antonio, TX, July 2002.
22. A. Grbic and G. V. Eleftheriades, "Experimental verification of backward-wave radiation from a negative refractive index metamaterial," J. Appl. Phys. **92**, 5930-5935 (2002).
23. S.Ramo, J. R. Whinnery and T. Van Duzer, *Fields and Waves in Communication Electronics*, 3rd ed., Toronto: John Wiley \& Sons, 1994, pp. 257-258.
24. A. Ishimaru, *Electromagnetic Wave Propagation, Radiation, and Scattering*, (Prentice Hall, Englewood Cliffs, NJ, 1991), pp. 165-169.
25. H. Kosaka, T. Kawashima, A. Tomita, M. Notomi, T. Tamamura, T. Sato, and S. Kawakami, "Superprism phenomena in photonic crystals," Phys. Rev. B **58**, R10096-10099 (1998).
26. M. Notomi, "Theory of light propagation in strongly modulated photonic crystals: Refractionlike behavior in the vicinity of the photonic band gap," Phys. Rev. B **62**, 10696 (2000).
27. C. Luo, S. G. Johnson, J. D. Joannopoulos, and J. B. Pendry, "All-angle negative refraction without negative effective index,'' Phys. Rev. B **65**, 201104(R) (2002).

1. Introduction

A material will be denoted throughout as a double positive (DPS) medium if its relative permittivity $\varepsilon_r = \varepsilon / \varepsilon_0 > 0$ and permeability $\mu_r = \mu / \mu_0 > 0$ are both positive. On the other hand, the relative permittivity and permeability are both negative in a double negative (DNG) medium, i.e., $\varepsilon_r < 0$ and $\mu_r < 0$. Consider a semi-infinite slab of metmaterial (an artificial realized material such as an DNG medium) embedded in free space. Consider an s-polarized (TE) incident wave (electric field perpendicular to the plane of incidence) that is incident on the slab at an angle of incidence θ_{inc} as shown in Fig. 1.

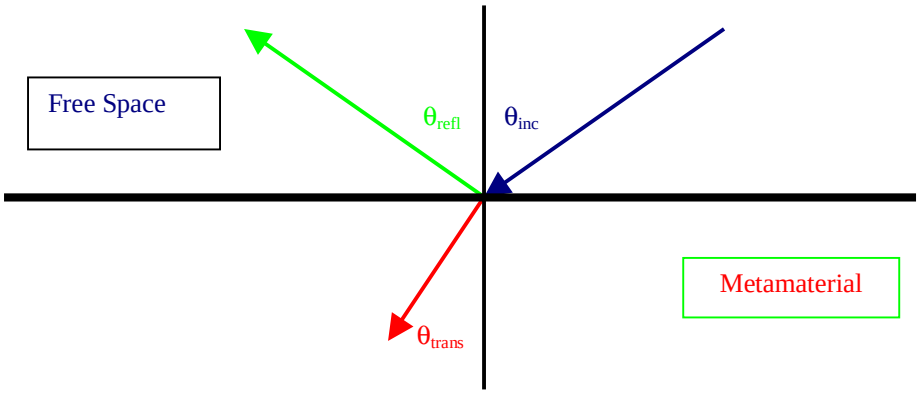

Fig. 1. Reflection and transmission configuration

#2157 - $15.00 US
Received February 03, 2003; Revised March 18, 2003

The reflected and transmitted waves are known to satisfy [1] the law of reflection and Snell's law:

$$\theta_{refl} = \theta_{inc} \tag{1}$$

$$n_{trans} \sin\theta_{trans} = n_{inc} \sin\theta_{inc} \tag{2}$$

where the index of refraction in either medium (*i*) is given by the expression

$$n_i = \sqrt{\frac{\varepsilon_i}{\varepsilon_0}}\sqrt{\frac{\mu_i}{\mu_0}} = \sqrt{\varepsilon_r}\sqrt{\mu_r} \tag{3}$$

where ε_0 and μ_0 are the free space permittivity and permeability. The reflection and transmission coefficients are given by the expressions

$$R = \frac{\eta_{trans}\cos\theta_{inc} - \eta_{inc}\cos\theta_{trans}}{\eta_{trans}\cos\theta_{inc} + \eta_{inc}\cos\theta_{trans}} \tag{4}$$

$$T = \frac{2\eta_{trans}\cos\theta_{inc}}{\eta_{trans}\cos\theta_{inc} + \eta_{inc}\cos\theta_{trans}} \tag{5}$$

where the wave impedance in either medium (*i*) is

$$\eta_i = \frac{\sqrt{\mu_i}}{\sqrt{\varepsilon_i}} \tag{6}$$

We will consider in most cases below a metamaterial that is DNG and is matched to free space. This means that $\varepsilon_r < 0$ and $\mu_r < 0$ so that $n < 0$ and that $\eta_{trans} = \eta_{inc}$. Consequently, for normal incidence one finds $R = 0$ and $T = 1$. Moreover, Snell's Law indicates that for any oblique angle of incidence onto the DNG interface, the transmitted angle will be negative. The existence and the effects of this negative angle of refraction have been discussed by several groups, e.g., [2]-[10].

Nonetheless, there has been some controversy about this negative angle of refraction [11] despite initial experimental verification [7] with 3D metamaterial constructs. More recent planar DNG transmission line [12] and related planar refractive cone experiments [13] have more clearly verified this effect. Matching of a DNG metamaterial to free space has been reported [14].

Here, in the hope to tie together the microwave regime with typical optical regime configurations, the interaction of pulsed Gaussian beams with DNG metamaterial slabs is studied numerically. The numerical simulations are obtained with the finite difference time domain (FDTD) method; the modeling environment is discussed in Section 2. The results for normally incident beam interactions with a DNG slab are presented in Section 3. It will be shown that a planar DNG slab does indeed focus the beam. The interactions of a obliquely incident beam with the matched DNG slab are considered in Section 4. The presence of the negative angle of refraction is clearly demonstrated. Both ultrafast pulsed (3-cycle) and continuous wave (CW) Gaussian beams are considered. Interesting effects including the generation of strong surface waves and backward waves in the $n = -1$ case are clearly demonstrated. Demonstration of the Goos-Hänchen effect for beams is discussed in Section 5. Both DPS and DNG media are considered. The lateral shift of the Gaussian beam upon total-

#2157 - $15.00 US Received February 03, 2003; Revised March 18, 2003

internal reflection that occurs in the DNG case is shown to be the reverse of the one for the DPS case. Conclusions and suggested practical applications for the negative refraction effects are considered in Sec. 6.

2. 2D-FDTD simulator

A two dimensional simulation environment with an s-polarized field was utilized for this beam interaction study. It was convenient and provided all of the necessary physics. The field components were assumed to be $H_x, E_y,$ and H_z.

As in [8], lossy Drude polarization and magnetization models were used to simulate the DNG medium. In the frequency domain, this means the permittivity and permeability were described as

$$\varepsilon(\omega) = \varepsilon_0\left(1-\frac{\omega_{pe}^2}{\omega(\omega+i\Gamma_e)}\right)$$
$$\mu(\omega) = \mu_0\left(1-\frac{\omega_{pm}^2}{\omega(\omega+i\Gamma_m)}\right) \tag{7}$$

The corresponding time domain equations for the polarization, P_y, and the normalized magnetization, $M_{nx} = M_x/\mu_0, M_{nz} = M_z/\mu_0$, fields are

$$\begin{aligned}
&\partial_t^2 P_y + \Gamma_e\,\partial_t P_y = \varepsilon_0\omega_{pe}^2 E_y\\
&\partial_t^2 M_{nx} + \Gamma_m\,\partial_t M_{nx} = \mu_0\omega_{pm}^2 H_x\\
&\partial_t^2 M_{nz} + \Gamma_m\,\partial_t M_{nz} = \mu_0\omega_{pm}^2 H_z
\end{aligned} \tag{8}$$

The normalized magnetization was introduced to make the electric and magnetic field equations completely symmetric. The Drude model is preferred over a Lorentz model for these studies since it provides a much wider bandwidth over which the negative values of the permittivity and permeability can be obtained. By introducing the electric and magnetic currents

$$\begin{aligned}
K_x &= \partial_t M_{nx}\\
K_z &= \partial_t M_{nz}\\
J_y &= \partial_t P_y
\end{aligned} \tag{9}$$

the field and current equations used to model the beam interaction with a DNG medium become

#2157 - $15.00 US Received February 03, 2003; Revised March 18, 2003

$$
\begin{aligned}
\partial_t H_x &= +\frac{1}{\mu_0}\left(\partial_z E_y - K_x\right) \\
\partial_t K_x + \Gamma_m K_x &= \mu_0 \omega_{pm}^2 H_x \\
\partial_t H_z &= -\frac{1}{\mu_0}\left(\partial_x E_y + K_z\right) \\
\partial_t K_z + \Gamma_m K_z &= \mu_0 \omega_{pm}^2 H_z \\
\partial_t E_y &= \frac{1}{\varepsilon_0}\left[\left(\partial_z H_x - \partial_x H_z\right) - J_y\right] \\
\partial_t J_y + \Gamma_e J_y &= \varepsilon_0 \omega_{pe}^2 E_y
\end{aligned}
\tag{10}
$$

In a DPS medium the corresponding field and current equation set is simply

$$
\begin{aligned}
\partial_t H_x &= +\frac{1}{\mu}\partial_z E_y \\
\partial_t H_z &= -\frac{1}{\mu}\partial_x E_y \\
\partial_t E_y &= \frac{1}{\varepsilon}\left(\partial_z H_x - \partial_x H_z\right)
\end{aligned}
\tag{11}
$$

The equation sets (10) and (11) were solved self-consistently and numerically with the FDTD approach [15], [16], i.e., these equations were discretized with a standard leap-frog in time, staggered grid approach. The electric field component was taken at the center of the square cells for integer time steps; the magnetic field components were taken along the cell edges for half-integer time steps. The electric and magnetic currents were located at the cell centers but with their time assignments opposite to the corresponding electric and magnetic field components, i.e., the magnetic current components were sampled at integer time steps and the electric current component was sampled at half-integer time steps. This allowed a FDTD stencil that properly simulated the matched medium conditions, i.e., this FDTD stencil produced the smallest numerical reflections because under matched conditions it produced numerical impedances associated with Eqs. (10) that coincided very closely with those associated with Eqs. (11). The time step $\Delta t = 22.39\, ps$ was set at 0.95 of the Courant value. The simulation space was truncated with a 10-cell layer Two Time Derivative Lorentz Material (2TDLM) model absorbing boundary condition [17], [18]. The simulation space was discretized into squares with a side length $\Delta = \lambda_0 / 100 = 100\, \mu m$. The simulation region (z vs x) for the normal incidence beam cases was $830\, cells \times 640\, cells$; for oblique incidence was $930\, cells \times 1040\, cells$ and for the Goos-Hänchen cases was $520\, cells \times 1040\, cells$. The simulation space was separated into total field and scattered field regions. The Gaussian beams were launched into the total field region using a total field - scattered field (TF-SF) formulation. This source approach has been used successfully for a variety of applications, e.g., in [19].

We note that Eqs. (11) and their numerical implementation will simulate a dispersionless DPS medium while the corresponding numerical implementation of Eqs. (10) will simulate a dispersive DNG medium. This difference does lead to some nuances when comparing the DNG and the DPS results below. However, since DNG media are necessarily dispersive [5], [8], the physics represented by Eqs. (10) is viewed as a practical model. Moreover, DPS media that are dispersionless are quite common (at least) at microwave frequencies. Thus, the DNG-

#2157 - $15.00 US Received February 03, 2003; Revised March 18, 2003

DPS comparisons made here are relevant to realistic situations that are encountered in potential experiments and applications.

Several matched slab cases were considered. In those cases the parameters for the electric and magnetic Drude models were identical, i.e., $\omega_{pe} = \omega_{pm} = \omega_p$ and $\Gamma_e = \Gamma_m = \Gamma$. In all cases, only low loss values were considered by setting $\Gamma = 10^{+8}\ s^{-1}$. In all cases, the center frequency of interest to define the index of refraction was chosen to be $f_0 = 30\ \text{GHz}$, corresponding to a free-space wavelength $\lambda_0 = 1.0\,cm$. This value was selected to connect these results to those presented in [8]. Note that all of the results to be presented can be achieved in a similar fashion at any desired set of microwave, millimeter, or optical frequencies with the appropriate frequency values in the Drude models and the corresponding FDTD simulation parameters. For the matched DNG $n = -1$ cases, these parameters were $\omega_p = 2\pi\sqrt{2}\, f_0 = 2.66573\times10^{11}\ rad/s$ and, hence, $\Gamma = 3.75\times10^{-4}\,\omega_p$. For the matched DNG $n = -6$ cases, these parameters were $\omega_p = 2\pi\sqrt{7}\, f_0 = 4.98712\times10^{11}\ rad/s$ and, hence, $\Gamma = 2.01\times10^{-4}\,\omega_p$. The real part of the index of refraction for these cases is shown in Fig. 2.

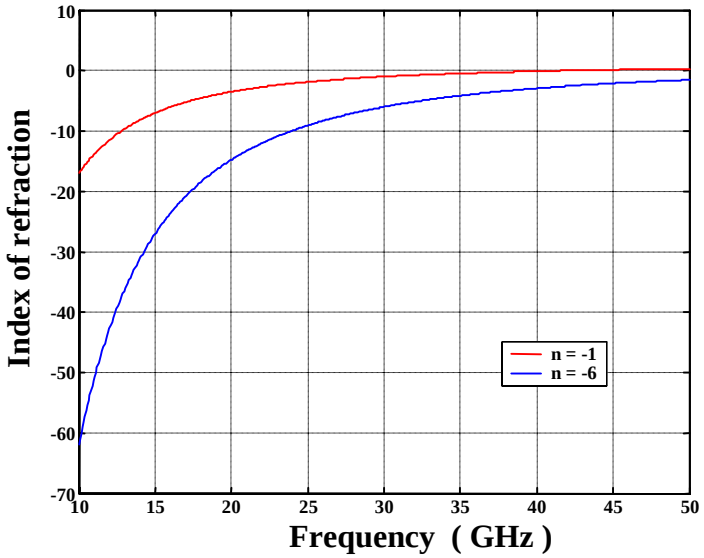

Fig. 2. Frequency response of the real part of the index of refraction associated with the lossy Drude models used in the FDTD simulations.

The input time signals were all multiple cycle *m-n-m* pulses given by the expressions

#2157 - $15.00 US
Received February 03, 2003; Revised March 18, 2003

$$f(t)=\begin{cases}0 & \text{for } t<0\\ \mathrm{g_{on}(t)}\sin(\omega \mathrm{t}) & \text{for } 0<t<mT_p\\ \sin(\omega \mathrm{t}) & \text{for } mT_p<t<(m+n)T_p\\ \mathrm{g_{off}(t)}\sin(\omega \mathrm{t}) & \text{for } (m+n)T_p<t<(m+n+m)T_p\\ 0 & \text{for } (m+n+m)T_p<t\end{cases} \tag{12}$$

where if the terms $x_{on}(t)=t/(mT_p)$ and $x_{off}(t)=\left[t-(m+n)T_p\right]/(mT_p)$, the continuous and two-derivative smooth functions

$$\begin{aligned} g_{on}(t)&=10x_{on}^3(t)-15x_{on}^4(t)+6x_{on}^5(t)\\ g_{off}(t)&=1-\left[10x_{off}^3(t)-15x_{off}^4(t)+6x_{off}^5(t)\right]\end{aligned} \tag{13}$$

These smooth excitation functions generate minimal noise as the waves are introduced into the FDTD simulation region. Each cycle has the period $T_p=1/f_0$. The function $g_{on}(t)$ goes smoothly from 0 to 1 in m-periods; the function $g_{off}(t)$ goes smoothly from 1 to 0 in m-periods. The function $f(t)$ thus turns on in m-periods, turns off in m-periods, and maintains a constant amplitude for its envelope over n-periods. All the CW cases below were turned on in 2-cycles and were then held constant for the entire simulation time, i.e., $m=2$ and $m+n>T_{total}$. The ultrafast input signals were $1-1-1$ (3-cycle) pulses. Thus the input time signals had their spectra centered on f_0 with either broad (3-cycle) or narrow (CW) bandwidths.

It is to be noted that the use of this purely numerical simulation approach to study the beam interaction has several advantages. Very complicated structures, as well as the DNG material, could be incorporated into the simulation region. Narrowband and broadband excitation pulses can be handled in the same simulation environment. However, and most importantly, there are no choices involved in defining derived quantities to explain the wave physics, e.g., no wave vector directions nor wave speeds are stipulated *a priori*. The FDTD simulator does not know which way the wave should refract at a DPS-DNG interface nor whether it should focus a beam in a DNG region or cause it to diverge. It simply calculates what is specified by Maxwell's equations there. In this manner, it provides an excellent approach to studying the wave physics associated with DNG metamaterials.

3. Normal incidence results

The normal incidence set of cases considered dealt with the issue of whether a planar DNG medium can focus the beam or not. The focal plane of the beam was taken to be the TF-SF boundary. The driving signals were all CW. The beam varies spatially as $\exp(-x^2/w_0^2)$ on that boundary, i.e., its amplitude falls to e^{-1} at its waist w_0. The beam that is generated has many wave vectors associated with it. Wave vectors off the beam axis point away from it for a diverging beam and towards it for a converging beam. Because it was expected that a DNG medium would have a negative index of refraction and would focus the beam, i.e., it would bend the wave vectors of a diverging beam back towards the beam axis, a strongly divergent beam was sought. A diffraction limited beam, whose waist was 50 cells ($\lambda_0/2$) in the TF-SF plane, was used. This beam had a near-to-far field distance of $\pi w_0^2/\lambda_0\approx\lambda_0$. The TF-SF boundary was thus set $2\lambda_0=200\,cells$ away from the DNG interface. This allowed sufficient

#2157 - $15.00 US Received February 03, 2003; Revised March 18, 2003

distance for the beam to diverge before it hit the interface. The DNG slab also had a depth of $2\lambda_0$; its width was $6\lambda_0 = 600\,cells$.

The beam propagating in free space is shown in Fig. 3. The electric field intensity in the simulation region is shown for one instant in time in each frame. The highest values are colored yellow; the lowest values are tan. Twenty-one snap-shots in time were captured at equal time intervals for 3000 time steps; the first frame represents the problem configuration at time zero. The DNG slab's boundary is superimposed on these frames to allow for comparisons to the actual DNG cases. The beam is clearly diverging as it propagates.

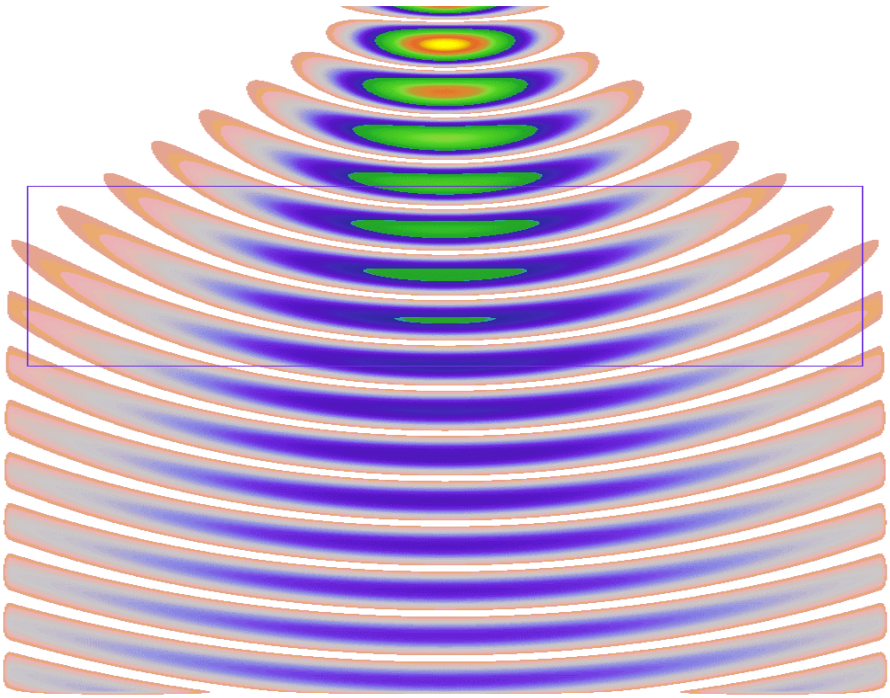

Fig. 3. (413 KB) Electric field intensity distribution for the normally incident Gaussian beam propagation in free space. The location of the slab region in the DNG simulations is shown.

The beam interaction with a matched DNG slab with $n = -1$ is shown in Fig. 4. The DNG slab was $2\lambda_0 = 200\,cells$ deep and it was $2\lambda_0 = 200\,cells$ away from the TF-SF plane. The focal plane of the source beam was taken at the TF-SF plane. The simulation was run for 5000 time steps and twenty-one snap-shots again were obtained. The frames show clearly that the planar DNG medium turns the diverging wave vectors towards the beam axis and, hence, acts as a lens to focus the beam. As shown in [8], with the source distance and the slab depth equal, the foci of the beam in the DNG slab and in the DPS medium beyond the DNG slab will coincide with $n = -1$ at a distance equal to the depth of the slab, i.e., the focal plane of the beam occurs at the rear face of the slab. This means that the DNG slab should ideally reproduce the beam at its rear face as it exists in the TF-SF plane. Note that if the source distance is much larger than the depth of the slab, no real foci occur and the convergence of the beam would again be maximized at the rear of the slab. This would be the anticipated configuration in many practical beam applications. The intensity of the electric field along the beam axis and along the front and back faces (as well as along every line shown in the first geometry slide of the movie) was sampled at the same time that each snap-shot was obtained.

#2157 - $15.00 US Received February 03, 2003; Revised March 18, 2003

The intensity along the beam axis at $t = 4500\,\Delta t$ is plotted in Fig. 5; the intensities along the front and back faces of the DNG slab are given in Fig. 6 for $t = 750\,\Delta t$ and $t = 4500\,\Delta t$, respectively. These times were selected because they are times in the FDTD simulation for the sinusoidal excitation at which the maximum values are realized at those beam axis points. The peaking of the beam towards the back face is evident in Fig. 5. The beam intensity is seen in Fig. 6 to have narrowed from a half width at half maximum of $50\,cells = 0.5\lambda_0$ at the front face to $30\,cells = 0.3\lambda_0$ at the back face. The intensity waist in the TF-SF plane is $w_0 / \sqrt{2} \approx 35\,cells$. The DNG slab has focused the beam slightly more than expected; the peak intensity is about 18% lower than its TF-SF plane value. These variances from the theoretical $n = -1$ result stem from the presence of additional wave processes, such as surface wave generation, and from dispersion and loss in the actual Drude model used to define the DNG slab in the FDTD simulations.

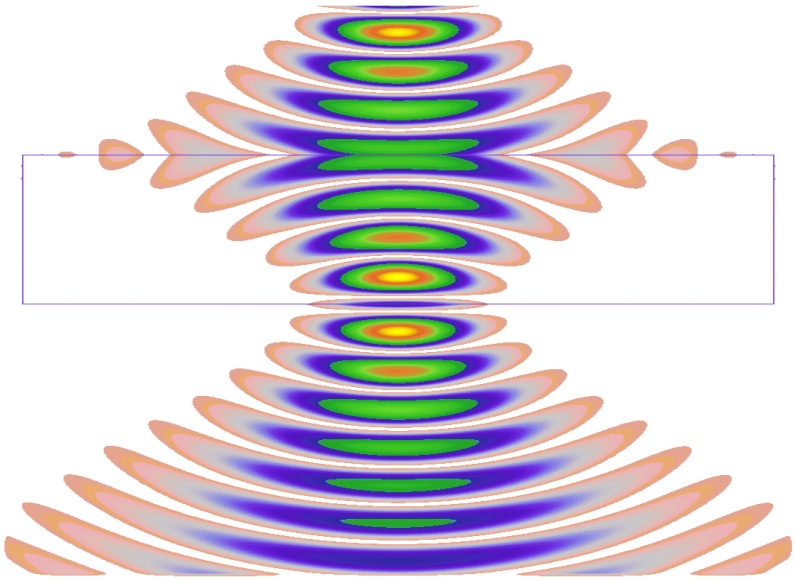

Fig. 4. (341 KB) Electric field intensity distribution for the normally incident Gaussian beam interaction with a DNG slab having $n = -1$. Focusing at the back surface is observed.

The corresponding results for the beam interacting with the matched DNG slab with $n = -6$ are shown in Figs. 7-9. The beam interaction with a matched DNG slab with $n = -6$ is shown in Fig. 7. The DNG slab was $2\lambda_0 = 200\,cells$ deep and it was $2\lambda_0 = 200\,cells$ away from the TF-SF plane. The focal plane of the source beam was again taken at the TF-SF plane. The simulation was run for 8000 time steps to allow for the slower speed of the beam in the DNG slab, and twenty-one snap-shots were again obtained. The intensity along the beam axis at $t = 4800\,\Delta t$ is plotted in Fig. 8; the intensities along the front and back faces of the DNG slab are given in Fig. 9 for $t = 750\,\Delta t$ and $t = 4800\,\Delta t$, respectively. In contrast to the $n = -1$ case, when the beam interacts with the matched DNG slab with $n = -6$, there is little focusing

#2157 - $15.00 US
Received February 03, 2003; Revised March 18, 2003

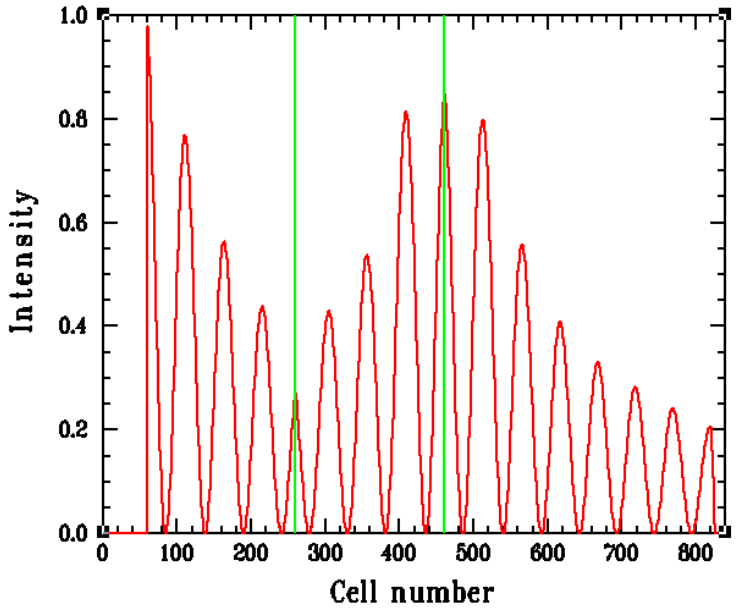

Fig. 5. Gaussian beam interaction with a DNG slab having $n=-1$. The intensity of the electric field along the beam axis is shown. The DNG slab front and back face locations are indicated by the green lines. Sharp discontinuities in the derivatives of the field across the DPS-DNG interface and focusing at the back surface are observed.

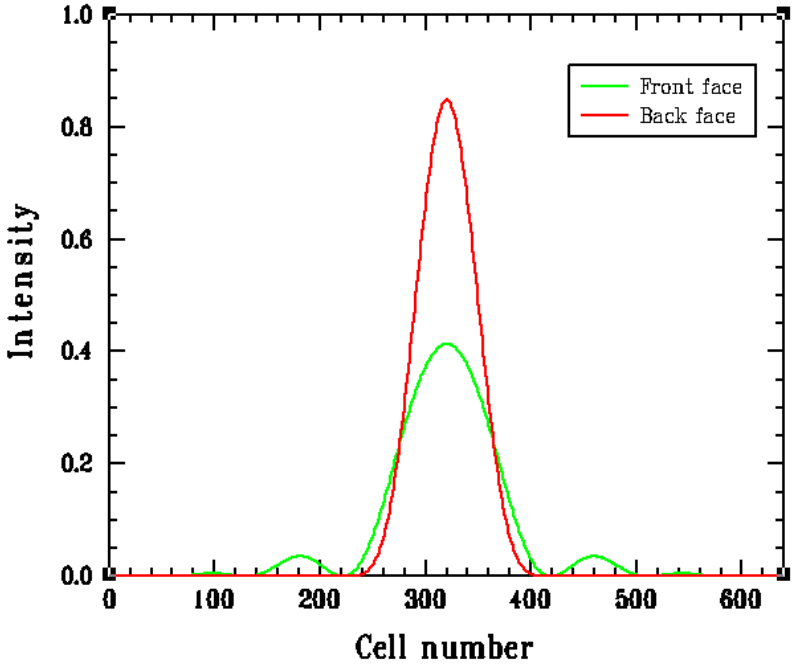

Fig. 6. Gaussian beam interaction with a DNG slab having $n=-1$. The intensity of the electric field along the front and back faces, orthogonal to the beam axis, are shown. Focusing and narrowing of the beam at the back surface are observed.

#2157 - $15.00 US
Received February 03, 2003; Revised March 18, 2003

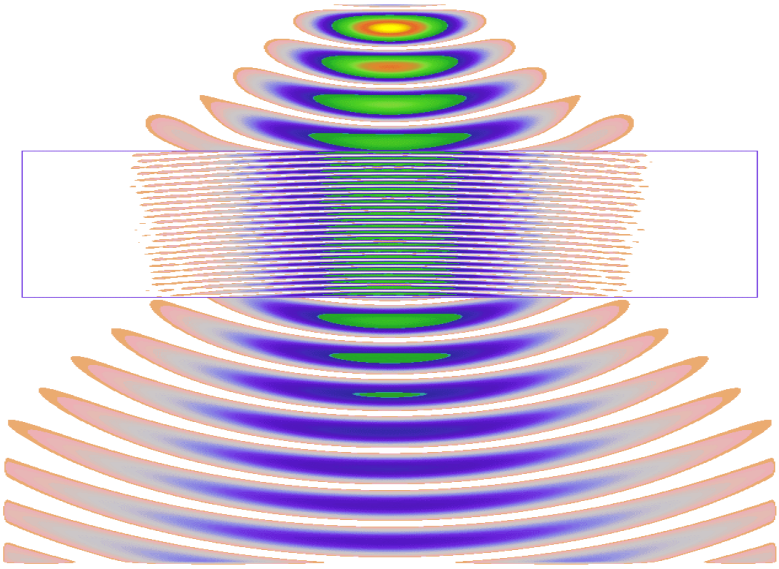

Fig. 7. (424 KB) Electric field intensity distribution for the normally incident Gaussian beam interaction with a DNG slab having $n=-6$. Channeling of the beam in the DNG slab is observed. The energy in the wings of the beam is seen to be directed towards the axis of the beam.

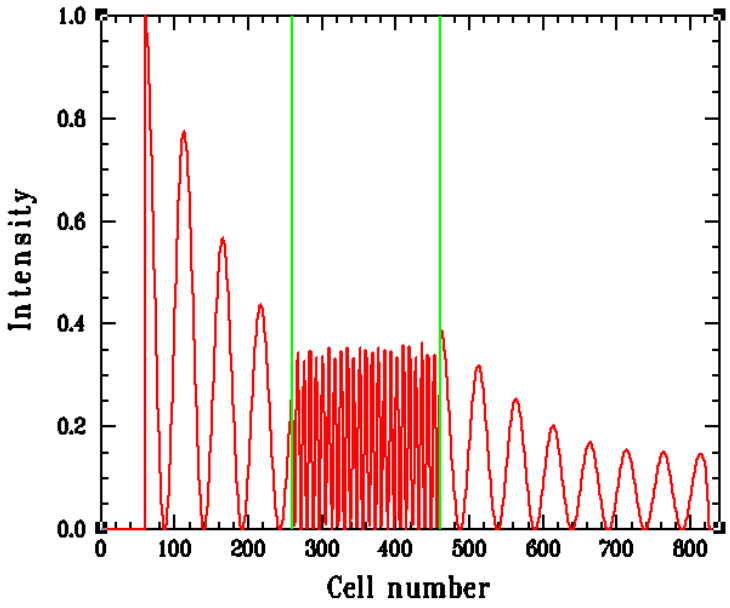

Fig. 8. Gaussian beam interaction with a DNG slab having $n=-6$. The intensity of the electric field along the beam axis is shown. The DNG slab front and back face locations are indicated by the green lines. Sharp discontinuities in the derivatives of the field across the DPS-DNG interface and maintenance of the center intensity are observed.

observed. The negative angles of refraction dictated by Snell's Law are shallower for this higher magnitude of the refractive index. Rather than a strong focusing, the medium channels

#2157 - $15.00 US
Received February 03, 2003; Revised March 18, 2003

power from the wings of the beam towards its axis, hence, maintains its amplitude as it propagates into the DNG medium. The fact that the wings of the beam feed its center portion can be perceived by the converging wave fronts shown in Fig. 7 at the edges of the beam in the DNG slab. The width of the beam at the back face is only very slightly narrower yielding only a slightly higher peak value there in comparison to its values at the front face. The strong axial compression of the beam caused by the (factor of 6) decrease in the wavelength in the $n = -6$ DNG slab is seen in Figs. 7 and 8.

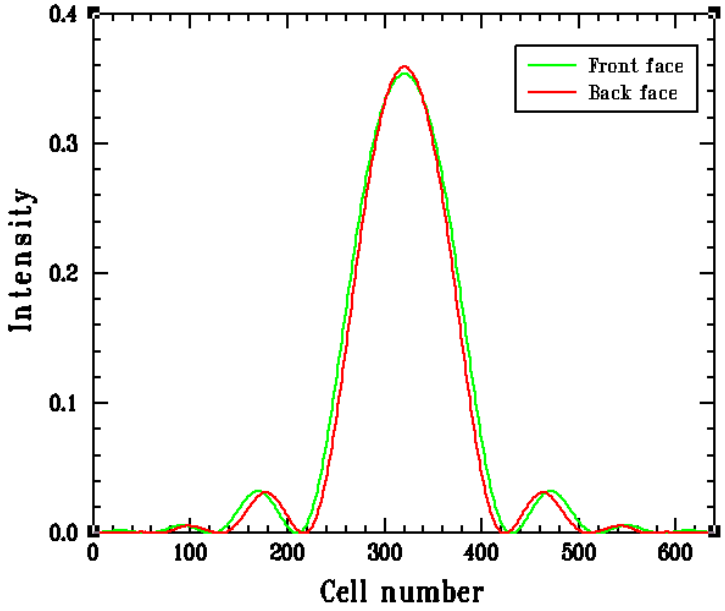

Fig. 9. Gaussian beam interaction with a DNG slab having $n = -6$. The intensity of the electric field along the front and back faces, orthogonal to the beam axis, are shown. There is only a slight narrowing in the width of the beam after its propagation through the entire DNG slab.

Note that in all the DNG cases the beam appears to diverge significantly once it leaves the DNG slab. The properties of the DNG medium hold the beam together as it propagates through the slab. Once it leaves the DNG slab, the beam must begin diverging, i.e., if the DNG slab focuses the beam as it enters, the same physics will cause the beam to diverge as it exits. The rate of divergence of the exiting beam will be determined by its original value and the properties and size of the DNG medium. Also note that a beam focused into a DNG slab will generate a diverging beam within the slab and a converging beam upon exit from the slab. This behavior has also been confirmed with the FDTD simulator.

4. Oblique incidence results

The oblique incidence set of cases considered dealt with the primary issue of whether a DNG medium will provide a negative angle of refraction or not. Both CW and 3-cycle pulse cases were simulated. The beam launched from the TF-SF plane had a waist of 100 cells (λ_0). The focal plane of the beam was orthogonal to the direction of propagation and centered at the TF-SF plane. The larger beam waist was selected in this study so that the DNG medium did not impact the beam shape as much as it propagated through the slab. The TF-SF boundary was set at $3\lambda_0 = 300\,cells$ away from the DNG interface. This allowed a sufficient distance for the

#2157 - $15.00 US
Received February 03, 2003; Revised March 18, 2003

entire beam associated with the 3-cycle pulse to be present in the simulation space before it interacted with the DNG slab. In all cases the angle of incidence of the beam was 20° and the slab depth was $2\lambda_0 = 200\,cells$. Note that for an angle of incidence $\theta_{inc} = 20^\circ$, $R = 0.031$ and $T = 0.969$. Hence, the reflected beam intensity was very small in comparison to the transmitted beam intensity.

The CW excitation pulse results for the $n = -1$ DNG slab are shown in Fig. 10. The simulation was run for 5000 time steps; twenty-one snap-shots in time were obtained at equal intervals. The negative angle of refraction is clearly seen. The beam was sampled along the front face of the slab and at the plane $200\,cells$ from the rear face. It was found that, as predicted by Snell's Law with a negative angle of refraction in the DNG medium, that the centroids of the beam at those planes were coincident. Despite the oblique nature of the propagation, the beam did focus the beam in the DNG slab towards its back face. The discontinuities in the derivatives of the fields at the DPS-DNG interfaces are displayed by the V-shaped patterns at the interfaces. Note that the reflected beam is not readily apparent because, as noted above, the reflection coefficient is quite small in this matched slab case. Also note that, as predicted in [20], [21], surface waves are generated as the beam interacts with the DPS-DNG interface. However, like the reflected waves, their intensity is small in comparison to the transmitted beam.

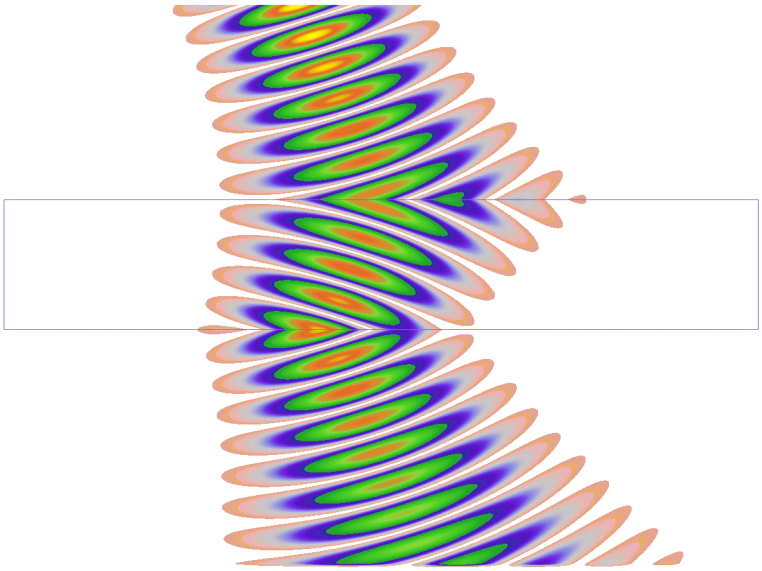

Fig. 10. (426 KB) Electric field intensity distribution for the interaction of a CW Gaussian beam that is incident at 20° to a DNG slab having $n = -1$. A negative angle of refraction equal and opposite to the angle of incidence is observed.

The results for the 3-cycle excitation pulse interaction of the $n = -1$ DNG slab are shown in Fig. 11. The simulation was run for 2500 time steps; twenty-six snap-shots in time were obtained at equal intervals. Several interesting effects can be highlighted. Notice that the ultrafast pulse generates a strong surface wave. Moreover, as this surface wave propagates away from the interaction region, it generates a backward wave [23] into the source side of the slab. These backward waves have been observed in [22]. Because of the broad bandwidth of the pulse, the dispersive effects of the Drude slab, the large angles involved, and the presence

#2157 - $15.00 US
Received February 03, 2003; Revised March 18, 2003

of several distinct wave processes, large distortions in the beam are also present in this example as it propagates through the DNG slab.

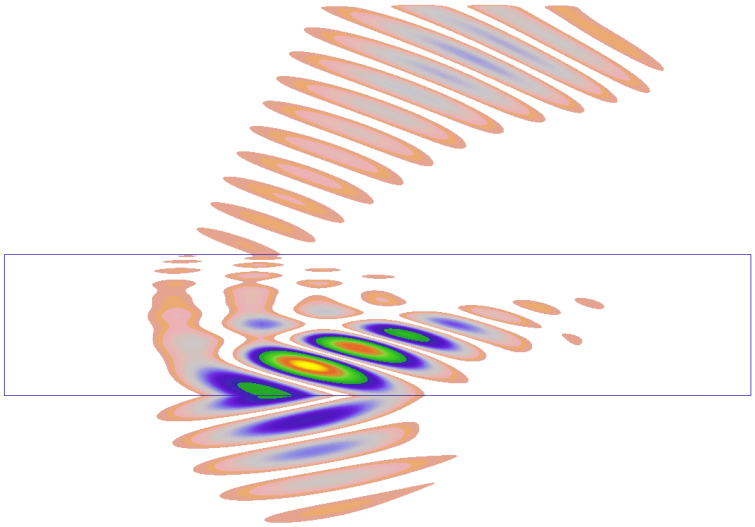

Fig. 11. (267 KB) Electric field intensity distribution for the interaction of a 3-cycle pulsed Gaussian beam that is incident at 20° to a DNG slab having $n=-1$. A negative angle of refraction of the transmitted pulsed beam is observed. A backward wave is generated at the front interface.

The CW excitation pulse results for the $n=-6$ DNG slab are shown in Fig. 12. The negative angle of refraction is again clearly seen. However, because of the change in wavelength in the DNG slab, the beam becomes highly compressed axially. Because the wave speed in the DNG slab correspondingly slows down by a factor of *6*, the simulation was run for 8000 time steps. Again, twenty-one snap-shots in time were obtained at equal intervals. The V-shaped patterns at the interfaces that display the discontinuities in the derivatives of the fields at the DPS-DNG interfaces are again clearly seen. Note that, as also predicted in [21], surface waves are not strongly generated as the beam interacts with the DPS-DNG interface when $n<0$ and $n\neq -1$. In contrast to the $n=-1$ case, there was little focusing in the DNG slab. Also note that the reflected beam is small because the DNG slab is again matched to the source region.

#2157 - $15.00 US
Received February 03, 2003; Revised March 18, 2003

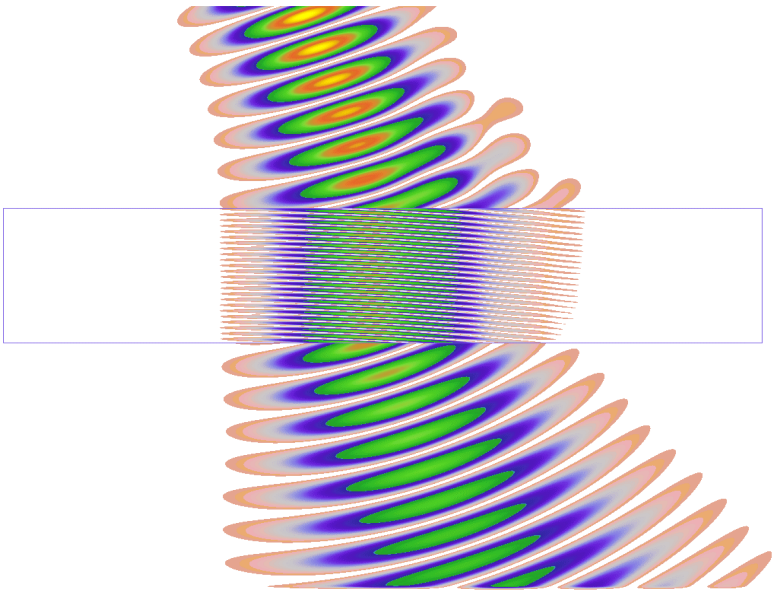

Fig. 12. (469 KB) Electric field intensity distribution for the interaction of a Gaussian beam that is incident at 20° to a DNG slab having $n=-6$. A shallow negative angle of refraction is observed. The beam is compressed in the DNG slab because of the higher refractive index.

The results for the 3-cycle excitation pulse interaction of the $n=-6$ DNG slab are shown in Fig. 13. The simulation was run for 5000 time steps; twenty-one snap-shots in time were obtained at equal intervals. Several interesting effects can be highlighted. Notice that even with its oblique angle of propagation through the slab and with its high degree of axial compression, the propagation of the pulsed beam was well-behaved. One can see the presence of a precursor beam leaving the slab ahead of the main pulse within the DNG medium. This results primarily from the broad bandwidth of the beam. Since there are high frequency components associated with the leading and trailing edges, they see a very different, smaller refractive index medium than does the center frequency. Finally, notice that its takes quite some time for the entire beam to return into the free space medium in back of the slab. This effect causes the ultrafast beam to become quite spread out in time. The beam again diverges once the centroid of the beam exits the DNG slab.

5. Goos-Hänchen effect

It is well-known that when a Gaussian beam is obliquely incident beyond the critical angle on an interface from a higher index of refraction DPS medium to a lower one, the centroid of the reflected Gaussian beam will experience a positive lateral shift along the interface from the purely specular reflection point of the centroid of the incident beam [24]. This Goos-Hänchen shift results from the wave vector direction dependence of the reflection coefficient (4). In particular, if x is the direction along the interface and z is the direction orthogonal to it, then the

#2157 - $15.00 US
Received February 03, 2003; Revised March 18, 2003

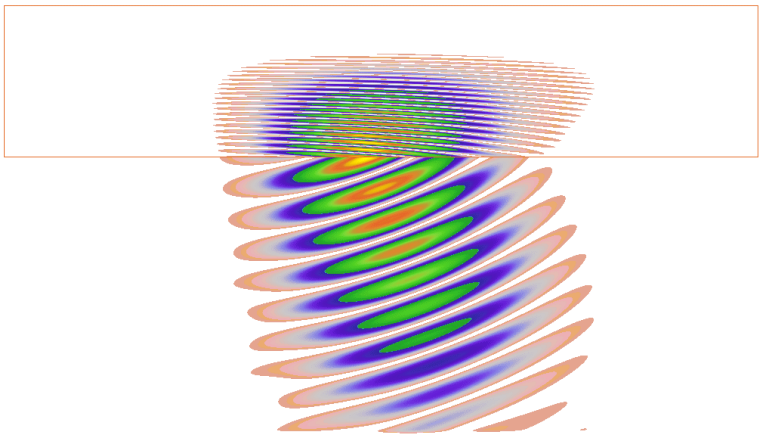

Fig. 13. (211 KB) Electric field intensity distribution for the interaction of a 3-cycle pulsed Gaussian beam that is incident at 20° to a DNG slab having $n=-6$. A negative angle of refraction and compression of the transmitted pulsed beam is observed.

corresponding wave vector components k_x and k_z are related as $k_z=\sqrt{\omega^2\varepsilon\mu-k_x^2}$ in both media. If k_{x0} represents the parallel component of the wave vector corresponding to the center of the incident beam, then an approximate expression for the reflected beam is [24]

$$E_y(x,z)=R(k_{x0})e^{ik_{x0}\Phi'(k_{x0})}E_{y,inc}(x-\Phi'(k_{x0}),z) \tag{14}$$

where the reflection coefficient (4) is re-written in the form

$$R(k_x)=\exp\left[-i\Phi(k_x)\right] \tag{15}$$

Equation (15) defines the phase function as $\Phi=i\ln R$; its derivative $\Phi'\equiv\partial\Phi/\partial k_x$ is then readily obtained. For an incident DPS medium with $\varepsilon_r=9.0$ and $\mu_r=1.0$ and for the transmission DPS medium with $\varepsilon_r=3.0$ and $\mu_r=1.0$, the critical angle is $\theta_{cr}=\sin^{-1}\left(n_2/n_1\right)=35.26^{\circ}$. Calculating the lateral shift $\Phi'(k_{x0})$ with a MatLab program for an angle of incidence of 40°, one finds that the shift should be $31.6\,cm$ for the frequency f_0. For the corresponding FDTD simulation, this would mean that the centroid of the reflected beam would be shifted approximately $32\,cells$ positively along the interface away from the incident beam center. If, on the other hand, the transmission medium is a DNG medium with $\varepsilon_r=-3.0$ and $\mu_r=-1.0$, then the wave vector components parallel to the interface in either

#2157 - $15.00 US
Received February 03, 2003; Revised March 18, 2003

medium must be equal, but the components normal to it are equal in magnitude and opposite in sign. This will cause the phase term Φ to have the opposite sign in the DNG medium case. Thus, one would expect the lateral shift to be $-32\,cm$, hence, $-32\,cells$ from the incident beam center on the interface. These theoretical results are pictorially represented in Fig. 14.

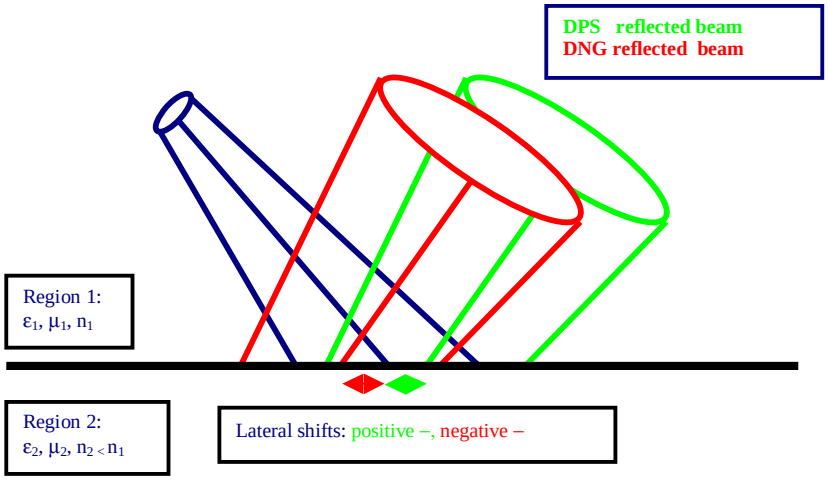

Fig. 14. A Gaussian beam obliquely incident from a higher refractive index magnitude medium to a lower one with an angle of incidence beyond the critical angle (blue) will generate a reflected beam that experiences a positive Goos-Hänchen lateral shift (green) in a DPS medium or a negative Goos-Hänchen lateral shift (red) in a DNG medium.

The FDTD simulation results for the Goos-Hänchen effect in the DPS and DNG media are shown, respectively, in Figs. 15 and 16. The simulation was run for 6000 time steps; twenty-one snap-shots in time were obtained at equal intervals between time steps 1000 and 6000. A CW Gaussian beam with a center frequency f_0 and with a λ_0 waist at the plane that is orthogonal to the beam axis and that intersects the front face of the slab at its center was launched from the TF-SF interface with a 40° angle of incidence in both cases. The TF-SF interface was $200\,cells$ from the front face of the slab. The slab was $200\,cells$ deep. The specular-like reflection process for the above-critical beam was realized. The presence of different beam centers is somewhat apparent when both figures are compared. To make this comparison clearer, the electric field intensity distribution measured at $t = 6000\,\Delta t$ along the plane two cells in front of the TF-SF plane for the DPS and for the DNG cases are shown in Figs. 17 and 18, respectively. The location in this plane of the initial beam center and the specularly reflected beam center are indicated by the vertical black lines. The location of the predicted Goos-Hänchen-shifted beam centers are indicated by the vertical green lines. Figures 17 and 18 clearly show the opposite lateral shifts between the DPS and the DNG cases. An analysis of the centroids of the reflected beams yielded approximately a $+31\,cell$ lateral shift in the DPS case and a $-21\,cell$ lateral shift in the DNG case, in reasonable agreement with the theoretical analysis. The corresponding movies show that the evanescent waves generated in the DPS slab penetrate further into the slab than they do in the DNG case. As could have been expected from the differences in the evanescent wave properties in DPS and DNG media, the

#2157 - $15.00 US
Received February 03, 2003; Revised March 18, 2003

wave interaction occurs primarily near the DNG interface. These corresponding movies also show a small delay before the reflected beam emerges from the interaction process.

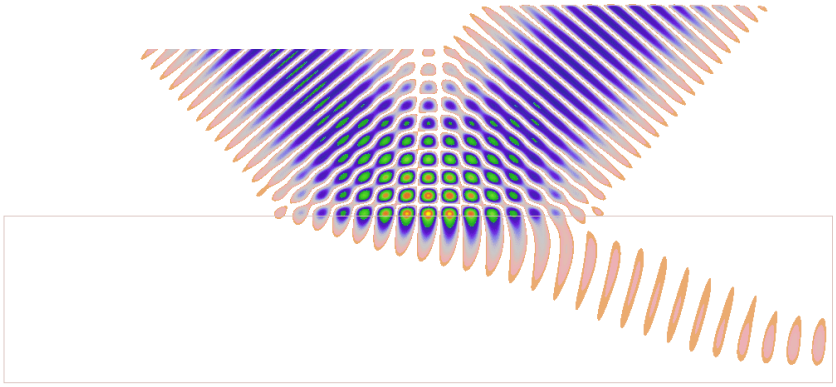

Fig. 15. (641 KB) Electric field intensity distribution for the interaction of a CW Gaussian beam that is incident at 40° in a DPS medium with $\varepsilon_r = 9.0$ and $\mu_r = +1$, i.e., $n = +3$ onto a DPS slab having $\varepsilon_r = +3.0$ and $\mu_r = +1$, i.e., $n = +\sqrt{3}$. The positive Goös-Hachen shift of this beam is observed. Some penetration of the beam into the slab occurs. The total field-scattered field boundary where the beam is generated is apparent. The total-internal-reflected beam propagates out of the FDTD total field region into the FDTD scattered field region as it passes this boundary.

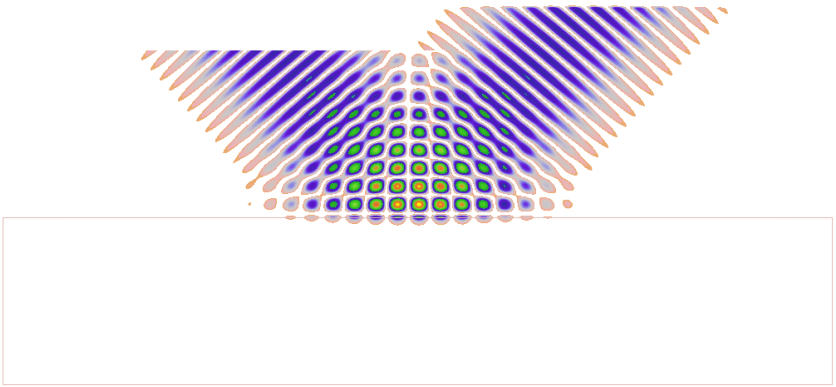

Fig. 16. (541 KB) Electric field intensity distribution for the interaction of a CW Gaussian beam that is incident at 40° in a DPS medium with $\varepsilon_r = 9.0$ and $\mu_r = +1$, i.e., $n = +3$ onto a DNG slab having $\varepsilon_r = -3.0$ and $\mu_r = -1$, i.e., $n = -\sqrt{3}$. The total field-scattered field boundary where the beam is generated is apparent. The total-internal-reflected beam propagates out of the FDTD total field region into the FDTD scattered field region as it passes this boundary.

#2157 - $15.00 US
Received February 03, 2003; Revised March 18, 2003

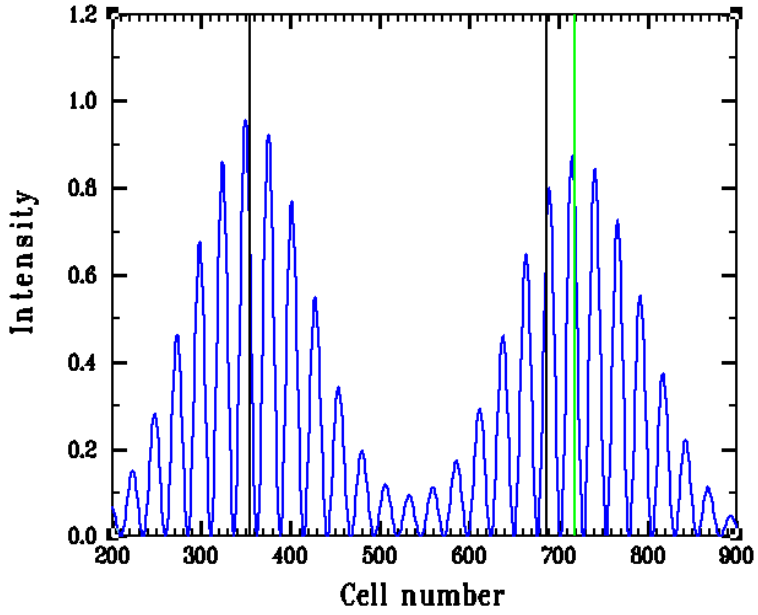

Fig. 17. The electric field intensity distribution measured at $t = 6000\Delta t$ at two cells in front of the TF-SF plane for the total internal reflection DPS slab case. The positions of the incident beam center and the specularly-reflected beam center are indicated by the vertical black lines. The theoretical positive Goös-Hachen shift is indicated by the vertical green line.

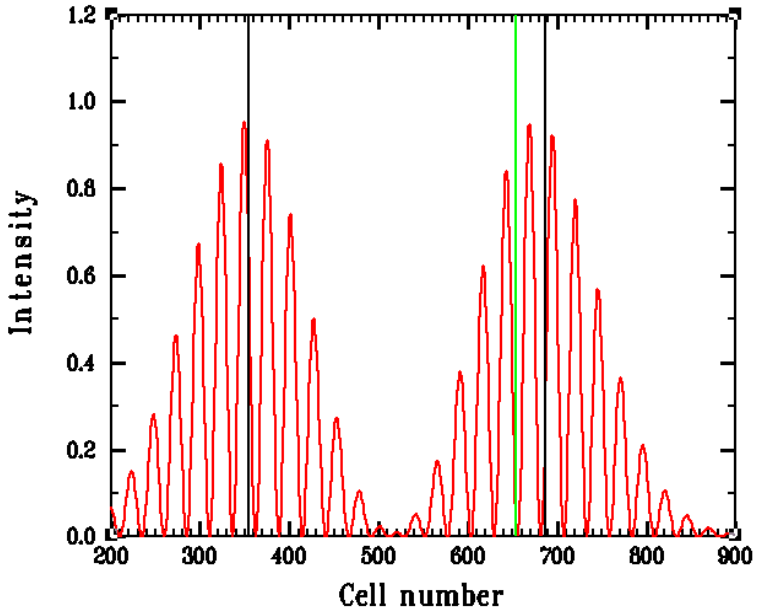

Fig. 18. The electric field intensity distribution measured at $t = 6000\Delta t$ at two cells in front of the TF-SF plane for the total internal reflection DNG slab case. The positions of the incident beam center and the specularly-reflected beam center are indicated by the vertical black lines. The theoretical negative Goös-Hachen shift is indicated by the vertical green line.

#2157 - $15.00 US
Received February 03, 2003; Revised March 18, 2003

6. Conclusions

The interactions of Gaussian beams with DPS and DNG slabs were investigated numerically. Both normal incidence and oblique incidence cases were considered. The normal incidence results demonstrated a focusing of the beams in a planar DNG slab. The oblique incidence results clearly showed the existence of a negative refractive angle behavior. The negative refractive effects were realized with 3-cycle and many-cycle pulsed Gaussian beams. A negative lateral Goos-Hänchen shift was demonstrated for a beyond-critical-angle Gaussian beam scattering from a DNG slab.

A number of interesting applications for DNG media arise from these results. The use of a DNG over-layer on a detector array could significantly enhance its behavior. Waves incident on the DNG over-layer could be focused to the back of the layer and, hence, onto the faces of the detector elements. Another potential application is for near-field scanning microscopy (NSOM). As shown in Figs. 4 and 5, there is a focal region just outside of the back face of the DNG slab. Since the field intensity has been concentrated there in a sub-wavelength region without a guiding structure, it could act as a much smaller aperture NSOM source than the typical tapered optical fiber probe and without similar aperture effects. The negative refractive angle behavior has already begun to be exploited through the DPS photonic band-gap super-prism effect, e.g., see [25-27]. The DNG media provide another form of metamaterial to realize those applications which include WDM switches and couplers.

Several of the predicted DNG metamaterial behaviors have been studied with a variety of microwave experiments. They have confirmed many theoretical and numerical analyses. Many more experiments are on-going and are needed. A variety of similar physics and engineering aspects of DNG metamaterials have been considered in the microwave, millimeter and optical regimes. Numerical experiments will be a dominating design environment for any eventual successful exploitation of these DNG metamaterial properties. Nonetheless, their eventual usefulness for many potential practical applications will depend greatly on clever fabrication concepts and implementations in those scenarios.

#2157 - $15.00 US Received February 03, 2003; Revised March 18, 2003